Magnetically focused 70 MeV proton minibeams for preclinical experiments combining a tandem accelerator and a 3 GHz linear post-accelerator

Michael Mayerhofer[a] and Gerd Datzmann
Universität der Bundeswehr München, Neubiberg, Germany

Alberto Degiovanni and Veliko Dimov
ADAM/AVO, Geneva, Switzerland

Günther Dollinger
Universität der Bundeswehr München, Neubiberg, Germany

(Received 21 June 2020; revised 28 February 2021; accepted for publication 14 March 2021; published 5 May 2021)

Purpose: Radiotherapy plays an important role for the treatment of tumor diseases in two-thirds of all cases, but it is limited by side effects in the surrounding healthy tissue. Proton minibeam radiotherapy (pMBRT) is a promising option to widen the therapeutic window for tumor control at reduced side effects. An accelerator concept based on an existing tandem Van de Graaff accelerator and a linac enables the focusing of 70 MeV protons to form minibeams with a size of only 0.1 mm for a preclinical small animal irradiation facility, while avoiding the cost of an RFQ injector.
Methods: The tandem accelerator provides a 16 MeV proton beam with a beam brightness of $B = 4\frac{\text{nA}}{\text{mm}^2\text{mrad}^2}$ as averaged from 5 μs long pulses with a flat top current of 17 μA at 200 Hz repetition rate. Subsequently, the protons are accelerated to 70 MeV by a 3 GHz linear post-accelerator consisting of two Side Coupled Drift Tube Linac (SCDTL) structures and four Coupled Cavity Linac (CCL) structures [design: AVO-ADAM S.A (Geneva, Switzerland)]. A 3 GHz buncher and four magnetic quadrupole lenses are placed between the tandem and the post-accelerator to maximize the transmission through the linac. A quadrupole triplet situated downstream of the linac structure focuses the protons into an area of (0.1 × 0.1) mm^2. The beam dynamics of the facility is optimized using the particle optics code TRACE three-dimensional (3D). Proton transmission through the facility is elaborated using the particle tracking code TRAVEL.
Results: A study about buncher amplitude and phase shift between buncher and linac is showing that 49% of all protons available from the tandem can be transported through the post-accelerator. A mean beam current up to 19 nA is expected within an area of (0.1 × 0.1) mm^2 at the beam focus.
Conclusion: An extension of existing tandem accelerators by commercially available 3 GHz structures is able to deliver a proton minibeam that serves all requirements to obtain proton minibeams to perform preclinical minibeam irradiations as it would be the case for a complete commercial 3 GHz injector-RFQ–linac combination. Due to the modularity of the linac structure, the irradiation facility can be extended to clinically relevant proton energies up to or above 200 MeV. © *2021 The Authors. Medical Physics published by Wiley Periodicals LLC on behalf of American Association of Physicists in Medicine.* [https://doi.org/10.1002/mp.14854]

Key words: magnetic minibeam focusing, particle optics codes TRACE 3-D and TRAVEL, preclinical irradiation facility, proton minibeam radiotherapy, pMBRT, tandem–linac accelerator combination

1. INTRODUCTION

With 478 000 new cases and 220,914 deaths from malignant tumors in 2016 in Germany and 14 million diagnoses worldwide,[1] the development of concepts for the successful treatment of tumor diseases remains one of the most important health challenges. Depending on the tumor type and location, radiation therapy is used in 60–70% of all cases.[2] Side effects induced by ionizing radiation in the surrounding healthy tissue are limiting the dose applied in the treatment volume. Therefore, the success of the treatment increases with a reduction of the delivered dose in normal tissue and thus reducing side effects in the healthy tissue in general.

The main tissue sparing effect in common radiotherapy modalities results from dose fractionation in time. Optimized radiotherapy, as for instance volumetric arc x-ray therapy (VMAT) and intensity-modulated radiation therapy (IMRT), additionally reduces side effects by a widespread dose distribution in the healthy tissues to reduce local doses while shaping the tumor dose to the desired value. Lower energy deposition and thus a further reduced dose in the healthy tissue are obtained by intensity-modulated charged particle therapy (IMPT). The linear energy transfer of the charged particles increases with depth and reaches a maximum close to the end of the range of the particles resulting in the so-called Bragg peak. Behind the tumor, nearly no dose is

deposited.[3,4] Compared to x-ray therapy, particle therapy utilizing for example protons or carbon ions usually offers the advantage that the therapeutic window, that compares the therapeutic dose in the tumor and the toxic dose in the healthy tissue, is substantially increased for deep-seated targets located close to critical organs.

Proton minibeam radiotherapy (pMBRT), as it was first published by Zlobinskaya et al.[5] and Prezado et al.,[6] allows tumor control and further reduces side effects by spatial fractionation effects compared to conventional proton therapy. Submillimeter-sized planar or pencil-like beams, called minibeams, are applied with a center-to-center spatial separation (ctc) much larger than the beam sigma of the individual minibeams at the entrance of the target. Typical values for ctc are between 1 and 20 mm[7] and for σ in the range between 0.02 and 0.4 mm. Thus, a substantial part of the gross irradiated field within the healthy tissue receives minor doses such that cell survival and repair capacity of the normal tissue in the irradiated field are strongly enhanced.[8] Within the tumor, a close to homogeneous irradiation can be achieved accordingly with two options: (a) unidirectional single field application and (b) interlacing minibeams:

Unidirectional applications (as discussed in detail by Zlobinskaya et al.,[5] Girst et al.,[9] and Sammer et al.[8]) may be the easiest way to perform proton minibeam therapy. The homogeneous dose distribution in the tumor is achieved by the natural lateral spreading of the protons from multiple small-angle scattering in the body, whereby the size of the minibeams increases with increasing depth until a homogeneous dose distribution is produced by the superposition of the individual minibeams within the tumor.[5,8–12]

In the second, much more advanced option, interlacing minibeams applied from two or more directions can offer a better sparing potential of the healthy tissue close to the tumor.[7] This second approach is technically more demanding to adjust the minibeams from the various directions to the required precision but can reduce side effects in the healthy tissue even close to the tumor.

Pencil minibeam spot scanning may have the best potential of tissue sparing compared to planar minibeams.[8,13] In the past, results from a human skin model[5] and a study within a mouse ear model[9,11,12] and in the rat brain[10] have shown the potential of pMBRT for reduced side effects compared to a homogeneous irradiation. Some of the mouse model studies have been performed at the Garching accelerator laboratory, where the SNAKE ion-microbeam setup can focus a 20 MeV proton minibeam through superconducting magnetic lenses into the required beam sizes.[8] In this work, the term beam size refers to the sigma (σ) of the one-dimensional projection of the two-dimensional geometric *X-Y* space particle distribution in an arbitrary direction (round beam). Pencil minibeams obtained from beam focusing (rather than by collimation) generate no extra dose by scattered protons from reactions within the collimator.[14] Another advantage of beam focusing is that the reduction of the initial beam current resulting from the need to illuminate a collimator surface larger than the holes in it can be avoided.[13] Beam sizes smaller than 0.1 mm and peak-to-valley dose ratios (PVDR) bigger than $10^4:1$ were already realized for an array of 20 MeV focused proton beams in a skin model study.[5]

Small animal studies with deeper located targets are the next step to evaluate the potential of pMBRT for clinical application. Therefore, accelerator concepts are needed to extend the proton range of about 4 mm (Munich tandem 20 MeV proton minibeams) to a range of 40 mm which does not limit any mouse or rat study. To estimate the required performance for a suitable preclinical irradiation facility, a simulation of a basic proton minibeam application was performed with the Geant4 toolkit TOPAS.[15] Figure 1 shows the interaction of a water phantom of size (44 × 24 × 24) mm with an array of 170 Gaussian 70 MeV proton minibeams without initial divergence [Figs. 1(a) and 1(b)] assuming a beam size of 90 μm and a *ctc* of 1.2 mm. The resulting dose distribution in a 40 μm thick *X-Z* layer [dotted line Fig. 1(a)] is shown in Fig. 1(b). The small *ctc* ensures a quasi-homogeneous lateral dose distribution within a hypothetic tumor ranging from $Z = 34$ mm to $Z = 41$ mm. Adding additional layers of lower proton energies in the same minibeam pattern would allow to cover this depth with a tumor dose distribution that fulfils all requirements of a homogeneous dose distribution in the tumor according to the ICRU requirements ($0.95 \cdot D < D < 1.07 \cdot D$).[16,17] The σ/ctc of 0.075 is close to the upper limit where nearly no side effects are expected in mouse skin tissue.[11] It has to be proven in further preclinical experiments how side effects in other tissues depend on the σ/ctc ratios. Thus, beam sizes ~90 μm or smaller and ctc distances in the 1 mm range are required to prove the principles of spatial fractionation schemes in future preclinical experiments.

In a previous study, at a proton energy of 20 MeV, beam sizes ~90 μm, and *ctc* ~1.8 mm, mouse ears showed almost no side effects for a PVDR > 540,[11] and therefore, the planned preclinical irradiation facility should offer similar PVDR values at the target entrance. The target area size (e.g., the front side of the tumor) of $X \times Y = 16$ mm × 13.5 mm results from the area covered by the individual channels [see Fig. 1(a)] and is comparable to field sizes already used to irradiate rat brains with minibeams.[18,19] The design goal for the beam scanning system of the preclinical test facility is $X \times Y = 30$ mm × 30 mm which is sufficient for small animal experiments. To ensure short irradiation times and dose rates > 40 Gy/s at any irradiation point that are actually discussed to reduce some side effects (FLASH irradiation), a beam current of ~4 nA is required to irradiate target areas of 100 mm^2 (estimated for a stopping power of 1 $\frac{keV}{\mu m}$).

This work validates a concept of a preclinical irradiation facility that will deliver focused proton pencil minibeams of variable energy up to a maximum of 70 MeV. An extension of this facility would even produce focused proton or heavy ion minibeams at clinically relevant energies of up to more than 200 MeV/μ.

The proposed system uses a conventional tandem Van de Graaff accelerator as it is available in many places around the world as an injector for an RF linear accelerator (RF – linac). The linac structure is based on the commercial AVO-ADAM

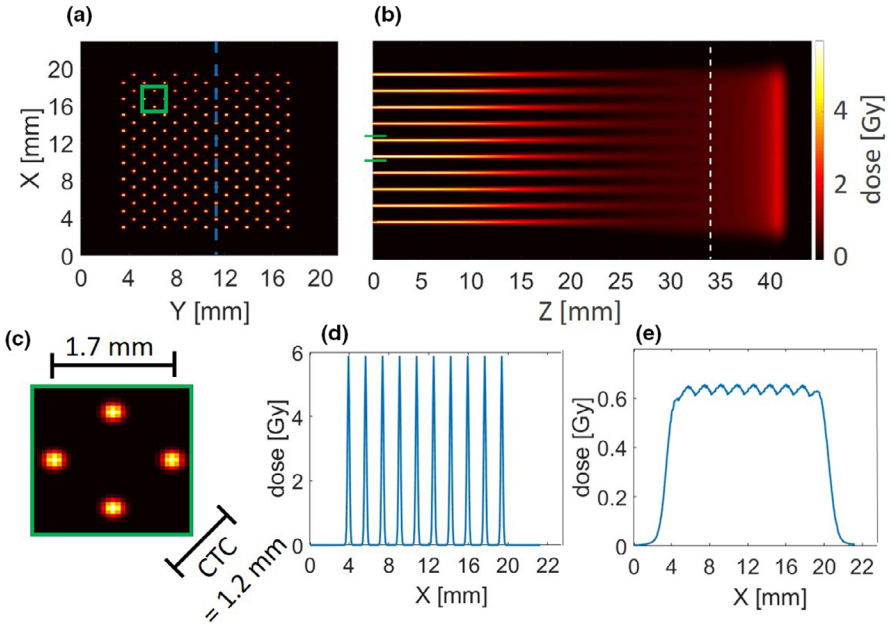

FIG. 1. Simulation of a water phantom irradiated with a quadratic array of 170 pencil Gaussian minibeams ($\sigma = 90$ μm) without initial divergence at a *ctc* = 1.2 mm of 70 MeV protons. (a) A cross section of an overall array of minibeams at the phantom entrance ($Z = 0$). (b) Dose distribution of a section (blue dashed line in a) in the phantom *X*-*Z* plane. Between $Z = 34$ mm (white dotted line in (b) and Bragg peak ($Z = 41$ mm) a homogeneous dose distribution in *X*-direction is obtained. (c) shows the unit cell of the beam array. (d) and (e) show the dose distributions in *X* direction for $Z = 0$ and $Z = 34$ mm.

LIGHT system.[20,21] Figure 2 shows the main components of the 24 m long LIGHT system which are briefly described in the following from left to right. A proton source provides a 40 keV beam which is chopped in pulses (5 μs at 200 Hz). Subsequently, the first linac section, a radio frequency quadrupole (RFQ) which serves as an injector for the following sections accelerates the beam to 5 MeV. The second linac section consists of four Side Coupled Drift Tube Linac (SCDTL) modules — as the ones designed within the TOPIMPLART project[22] — which accelerate the protons to an energy of 37.5 MeV. The final proton energy of 230 MeV is achieved by the third linac section, consisting of 15 Coupled Cavity Linac (CCL) structures (designed by AVO-ADAM). The linac modules operating at 3 GHz and are driven by klystrons (see white boxes in Fig. 2) delivering an RF peak power of 7.5 MW (5 μs at 200 Hz). Due to the filling time of 2 μs, which is required to build up the fields in the linac structure, 3 μs of the 5 μs long RF pulse are effectively used for acceleration up to now. However, the duty cycle of the system can be improved by using an RF power supply offering longer pulses or a higher repetition rates. No degrader is needed for the variation of the beam energy. This and the fact that almost no beam current is lost in the structures reduces the costs for shielding significantly compared to a cyclotron-based facility.[23]

In this paper, beam parameters as obtained at the Munich tandem accelerator (maximum terminal voltage: 14 MV) are used for beam transport calculations. A sketch of the facility is shown in Fig. 3. A 16 MeV proton beam of high brightness is provided by the tandem accelerator operated with a terminal voltage of 8 MV and is chopped to the pulse length accepted by the linac (5 μs long pulses at 200 Hz repetition rate[20]). Although the tandem accelerator can provide up to 28 MeV protons as an injector, 16 MeV is preferred in practical applications to guarantee current stability in continuous operation and to avoid generation of large radiation background and activation at the interface to the linac where a certain fraction of the beam will be dumped in copper and stainless steel structures.

The longitudinal phase space of the beam coming from the tandem is matched to the RF pulse structure of the linac by a 3 GHz buncher. The transverse phase space is cut by a round aperture and transformed using a magnetic quadrupole quadruplet to fit into the linac acceptance. Acceleration voltages of the linac sections are adjusted to meet the required energy for the proton minibeam irradiation. The beam is focused after the post-accelerator to form the proton minibeam at a small animal irradiation facility.

This concept will allow to extend the proton range to about 40 mm (for 70 MeV protons[24]). The proposed approach allows an upgrade of an existing tandem, at reduced cost, using the medium energy section of the linac and starting the RF acceleration at 16 MeV, rather than installing the full front-end accelerator chain (including source, RFQ, and the first modules of 3 GHz linac). The details of the proposed system and the beam parameters as simulated by multi-particle tracking calculations are shown in the following. For the sake of completeness, they are also compared to those of a short version of a commercially available RFQ–linac combination at 70 MeV as it may be set up when a dedicated system is intended to be installed without a pre-existent injector.

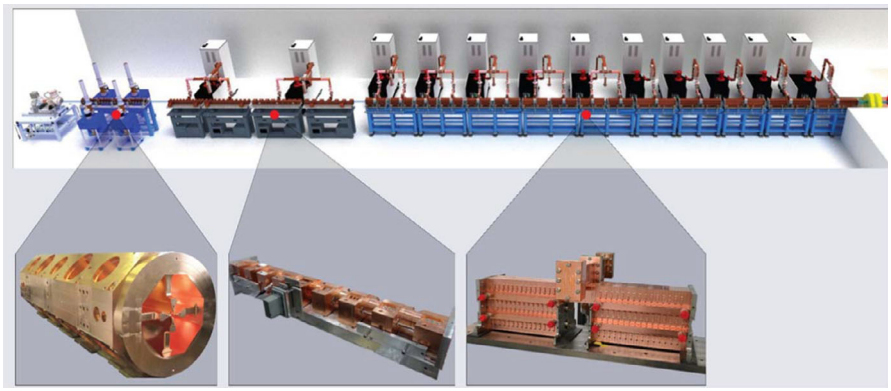

FIG. 2. AVO-ADAM LIGHT 3 GHz system.[20] From left to right: 40 keV proton source (5 μs at 200 Hz), radio frequency quadrupole (RFQ) (first highlighted image), output energy: 5 MeV, four Side Coupled Drift Tube Linac (SCDTL) modules (second highlighted image), output energy: 37.5 MeV and 15 Coupled Cavity Linac (CCL) structures (third highlighted image), output energy: 230 MeV. In the background, the klystrons supplying the linac structures with 7.5 MW RF- peak power. [Color figure can be viewed at wileyonlinelibrary.com]

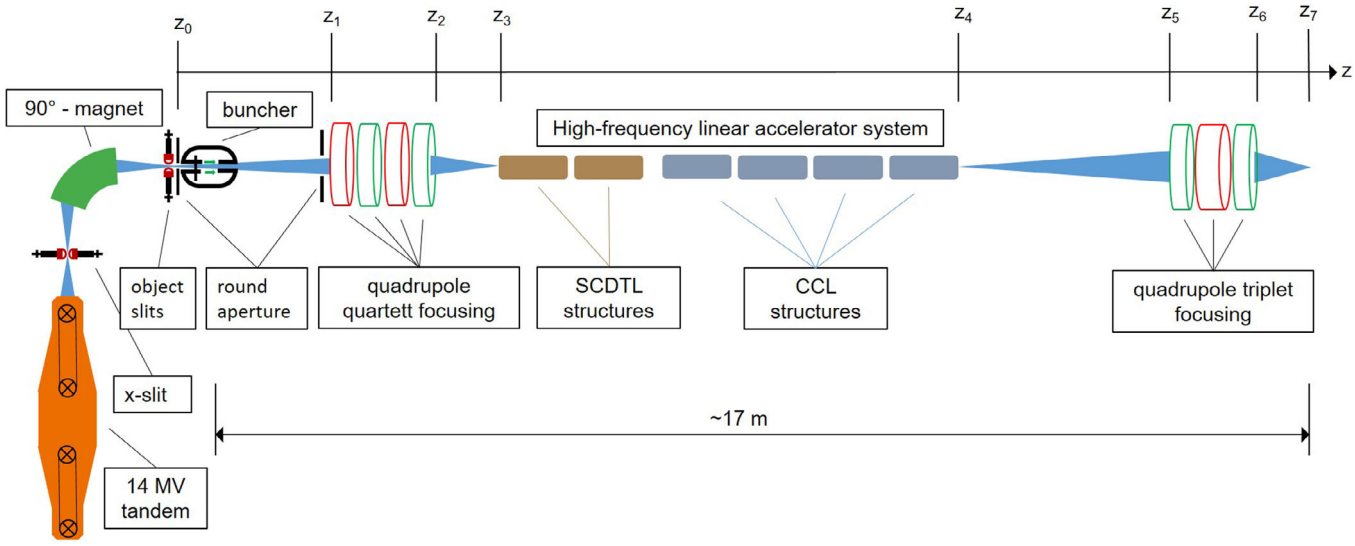

FIG. 3. Concept of the proposed pre-clinical proton therapy system to form sub-millimeter proton beams at 70 MeV. [Color figure can be viewed at wileyonlinelibrary.com]

2. MATERIALS AND METHODS

The Munich tandem accelerator situated at the Maier Leibnitz Laboratory in Garching[25] is able to provide a 16 MeV proton beam with a relative energy spread of 10^{-4} stabilized via slit current analysis behind a double focusing 90° deflecting magnet. The beam can be chopped to 5 μs pulse length at 200 Hz repetition rate at the low energy side of the tandem[8] to adapt to the duty cycle of the 3 GHz linear post-accelerator considered here to provide up to 70 MeV protons for preclinical experiments. In a test experiment[26] where the beam was cut with a rectangular slit system in *X*-*Y* and *X*′-*Y*′, an average proton beam current of $I = 8.5$ nA at a full 4D transverse emittance $\epsilon = 4.2$ mm^2 mrad^2 (normalized emittance $\epsilon_n = 0.15$ mm^2 mrad^2) was achieved. Due to the duty factor of $5 \cdot 10^{-4}$ (5 μs at 100 Hz), the measured peak beam current at the flat top was 17 μA. For a duty factor of 10^{-3} (5 μs at 200 Hz) as intended for the presented preclinical irradiation facility, these values result in an averaged beam brightness of the chopped beam of:

$$B = \frac{I}{\varepsilon} = 4.0 \frac{\text{nA}}{\text{mm}^2\,\text{mrad}^2}, \quad (1)$$

and a normalized brightness of:

$$B_n = \frac{I}{\varepsilon_n} = 113 \frac{\text{nA}}{\text{mm}^2\,\text{mrad}^2} \quad (2)$$

A focus point downstream of the 90° magnet, marked as z_0 in Fig. 3, serves as the starting point of the proposed post-accelerator and beam delivery system for preclinical experiments. The beam is assumed to be cut by round apertures at this starting point and downstream in front of a magnetic lens system at z_1 to define the beam size and divergence of the beam. The magnetic lens system consists of a quadrupole quadruplet to adapt the transverse phase space of the incoming bunched tandem beam to the phase space accepted by the

linac at z_3 plane. A buncher unit is installed behind the round aperture at z_0 to optimize the longitudinal phase space injected into the post-accelerator. The buncher is operated at the same frequency as the linac (f_{bunch} = 3 GHz). The buncher amplitude and phase are adjusted to maximize the transmission through the linac. After the buncher, some linac structures from the LIGHT accelerator[20,21] are adapted consisting of two Side Coupled Drift Tube Linac (SCDTL) structures and four Coupled Cavity Linac (CCL) structures. The maximum energy obtained with these structures is 70 MeV as required for preclinical experiments. After the post-accelerator, an additional focusing system consisting of a quadrupole triplet at z_5 is used to generate beam size of about 90 μm at z_7.

In the following, the details of the post-accelerator and the beam transport concept are presented. Beam transport simulations allow estimating beam current and beam quality at the target station at z_7 giving information whether and under which conditions preclinical proton minibeam experiments can be performed. The distance between a point z_a and a point z_b is represented in the following by the abbreviation z_{ab}.

2.A. Definition of the initial phase space

In order to calculate the beam transmission through the post-accelerator into a beam spot square of 0.1 mm × 0.1 mm, the following beam parameters from the Munich tandem Van de Graaff accelerator are assumed at z_0:

a For the transverse phase space: a circular beam of radius $X_R = Y_R = 1$ mm and a circular divergence of $X'_R = Y'_R = 1$mrad as cut by circular apertures at z_0 and z_3 from a larger, homogeneous beam. Thus, the protons are assumed to be uniformly distributed in the $X - Y$ and the $X' - Y'$ projection of the four-dimensional phase space.
b For the longitudinal phase space: a uniformly distributed DC beam of full phase width $\Delta\varphi = \pm 180°$ (at 3 GHz) and a full energy spread $\Delta E/E_0 = \pm 0.01\%$ of the initial kinetic energy E_0 = 16 MeV of the proton beam.

The beam parameters are summarized in Table I. Projections of the six-dimensional (6D) phase space on the X–X', Y–Y', $E - \varphi$ and the two-dimensional geometrical space X–Y of the particle distribution from the tandem accelerator at z_0 are plotted in Fig. 4 (number of particles N_P = 1000 000). These particle distributions are used as input data for all beam transport simulations through the "preclinical minibeam system." An averaged beam current of $I_p = B \cdot \epsilon$ = 40 nA would be available for the 5 μs beam pulses at a 200 Hz repetition rate as calculated from the beam brightness B [Eq. (1)] and the four-dimensional transverse emittance ϵ:

$$\varepsilon = 1\pi^2\,\mathrm{mm}^2\,\mathrm{mrad}^2 \tag{3}$$

The normalized emittance ε_n is:

$$\varepsilon = 0.034\pi^2\,\mathrm{mm}^2\,\mathrm{mrad}^2 \tag{4}$$

TABLE I. Parameters of the six-dimensional phase space at the focus point (z_0). Protons are uniformly distributed in the X-Y, in the X'–Y', and in the ΔE–Δφ projections.

Transverse phase space	Dimension	X_R[mm]	±1
		Y_R[mm]	±1
	Divergence	X'_R[mrad]	±1
		Y'_R[mrad]	±1
Longitudinal phase space	Phase spread	$\Delta\varphi$[°]	±180
	Energy spread	$\Delta E/E_0$[%]	±0.01
Average kinetic energy		$\mathbf{E_0}$ [MeV]	16

2.B. High frequency linear post-accelerator system

The linear post-accelerator acts as a central, fixed element in this concept study. Its influence on the simulated particles is given completely by a description of its accelerating structures from the LIGHT-system as provided by AVO-ADAM.[21]

2.C. Medium energy beam transfer line

The overall phase acceptance of the 3 GHz linac is 58.5° at maximum.[27] This corresponds to 55 ps within one RF cycle of 333 ps. Since the tandem accelerator provides a DC-beam, a buncher is introduced to optimize the beam transmission through the linac. By introducing a correlation between phase and energy, the buncher compresses a substantial amount of particles into the short phase acceptance window of the post-accelerator while widening the energy spread.

The buncher cavity uses a sinusoidal voltage at the resonant frequency of 3 GHz in a cavity resonator with one or more gaps. As for any kind of buncher in particle optics, the protons are decelerated if they enter the gap before the zero crossing and accelerated if they enter later than the zero crossing of the voltage. Through the induced proton velocities modulation, the bunch length is minimized after a certain drift distance forming a focus in the longitudinal phase space. This focus is intended to be situated close to the entrance of the linac. The main objectives of the beam transport studies in order to calculate optimized beam parameters were defining (a) the drift distance between buncher and linac (z_{03}), (b) the buncher voltage amplitude U_b, and (c) the phase offset $\Delta\varphi_S$ with respect to the 3 GHz electromagnetic wave of the linac.

The geometric structure of the considered buncher is similar to that of common RF standing wave accelerators.[28] Since the frequency of the buncher will be synchronized to the 3 GHz frequency of the LIGHT system, the buncher could in principle be supplied with a fraction of energy by the available klystrons. Otherwise, it can be driven by an extra power supply operated at a defined phase relative to the accelerating cavities. Bunchers of these resonator frequencies have already been developed and tested by Picardi et al.[29,30] Buncher structures adapted to all requirements are presented in a forthcoming paper.[31]

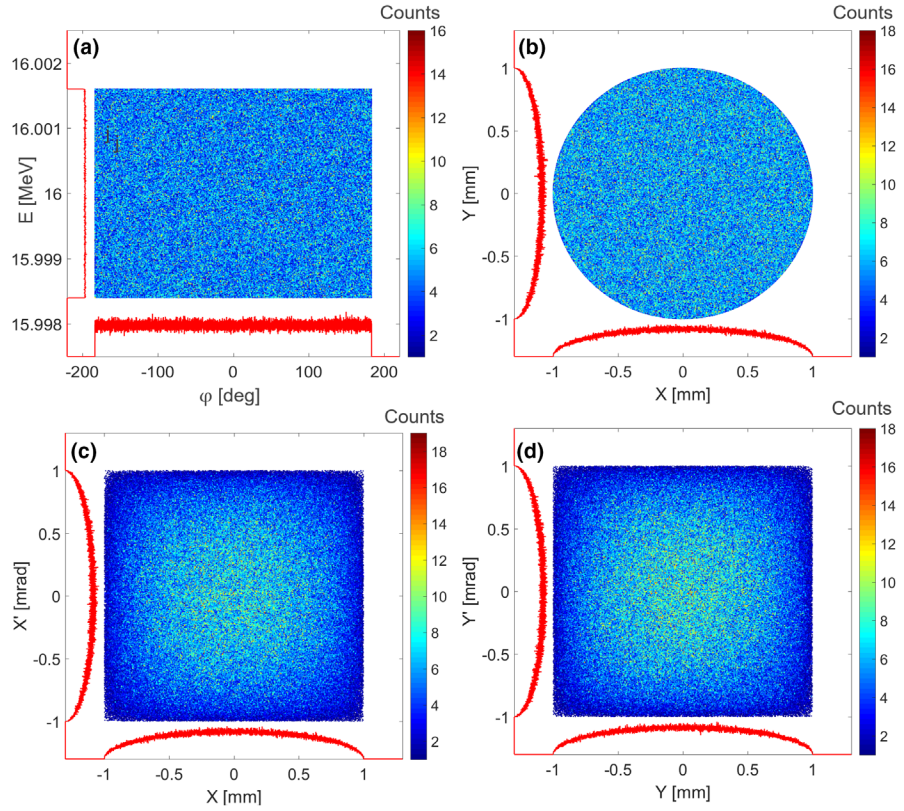

FIG. 4. Two-dimensional projections of the six-dimensional phase space distribution of the 1,000,000 protons used as input for ray tracing calculations at injection point z_0 (see Fig. 3) (a) ΔE-φ, (b) *X-Y* (c) *X–X′*, (d) *Y–Y′*. The projections of the particle distributions on the respective axes of the individual beam parameters are shown in red. The DC beam is uniformly distributed in the *X-Y*, the X′–Y′, and the ΔE-Δφ projection of the six-dimensional phase space resulting in an inhomogeneous distribution in *X–X′* and *Y–Y′*.

An electromagnetic quadrupole quadruplet with its entrance at z_1 is used to match the transverse phase space of the proton beam coming from the tandem accelerator with that accepted by the linac.

2.D. Beam transport simulations

In this work, two different simulation tools are used to develop and evaluate the concept of the accelerator facility:

TRACE 3-D,[32] a first-order beam dynamic program from the Los Alamos National Laboratory to determine the envelopes of a bunched beam at a certain point of the beamline.

For the studies shown here, the quadrupole quadruplet at z_1 and the quadrupole triplet at z_5 (magnetic field strength, length of the quadrupoles, and distance between the quadrupoles), the buncher cavity (voltage U_b) and all drift spaces (length) were designed with TRACE-3D to determine the size of the preclinical irradiation facility. To achieve an optimized transmission through the linac a matching process to the 6D phase space at point z_3 accepted by the linac was performed with TRACE-3D where the magnetic field strengths of the quadrupole magnets placed between buncher and linear accelerator at (z_1) are used as free parameters. Another matching routine is used for the magnetic triplet behind the post-accelerator (z_5). The main goal was to obtain a close to symmetric beam size of about 90 μm at a focal plane z_7. The magnetic field strengths of the individual quadrupoles of the triplet were selected as free parameters for this process.

In the second step, after the first-order optimization, the particle tracking code **TRAVEL**[33] is used including an extension by a graphical user interface PATH MANAGER as developed at CERN. TRAVEL is a multi-particle tracking code which allows the user to introduce higher order calculation and space charge effects. The description of the beamline included all the elements shown in Fig. 3 starting from z_0 up to z_7.

The particle distribution and beam transmission into the focus point z_7 of the preclinical irradiation facility optimized in TRACE-3D are then simulated with TRAVEL. The transmission is determined by the fraction of transmitted particles into the target area for a desired beam spot square of 0.1 mm × 0.1 mm at the focus z_7. The particle distribution is evaluated by comparing histograms of the *X* and *Y* projections of these particle distributions to draw conclusions about the shape and the fraction of the beam in the halo.

As input for the simulations, we used the 6D phase space particle distribution already described and illustrated in Fig. 4, modeled as a uniformly distributed ensemble of one million particles within the phase space limits reported in Table I. For each change of the buncher unit parameters, like amplitude U_b, phase difference Δφ between buncher and linac and drift length between buncher and linac, the full line

is rematched with TRACE 3D and the particle distribution and transmission up to z_7 is calculated by TRAVEL.

3. RESULTS AND DISCUSSION

3.A. Beam matching to the post-accelerator

In the first step, the acceptance of the post-accelerator structure at its entrance (z_3 in Fig. 3) was obtained by performing an acceptance study with TRAVEL. For this study, a phase space distribution of the protons at z_3 was assumed much wider for all dimensions than what the accelerator can accept. A DC beam of full angle $\Delta\varphi = \pm 180°$ and a full energy spread $\Delta E/E_0 = \pm 5\%$ was taken for the longitudinal phase space. For the transverse phase space, a circular beam of radius $X_{max} = Y_{max} = 5$ mm and a circular divergence cut-off of $X'_{max} = Y'_{max} = 15$ mrad was considered. Only protons transported through the linear accelerator to its exit at z_4 are marked in their original position in the 6D phase space at the entrance of the accelerator at z_3 (Fig. 5).

In the second step, the phase space of the proton beam from the tandem accelerator (see Fig. 4) was transformed to fit into to the acceptance of the linac by the buncher at z_0 and the quadrupole quadruplet at z_1. The optimization of the matching was performed by varying buncher and geometry settings (shown in Section 3.B) and checking the transmission from the number of particles transported through the linac from an injected total of $N_P = 10^6$ particles.

As an example, Fig. 6 shows the particle distribution in the transverse phase space *(colored)* as transported from the tandem accelerator assuming the 4D emittance of the tandem of Fig. 4, and a buncher amplitude $U_b = 35$ kV ($z_{03} = 3.27$ m). The quadrupole quadruplet allows a reasonably good matching of the transverse phase spaces between the tandem output and the acceptance of the linac represented by the gray dots in Fig. 6. The resulting quadrupole lengths, distances, and magnetic field gradients are shown in Fig. 7 and Table II.

The particle distribution in the longitudinal phase space at z_0 in front of the buncher is shown in Fig. 8(a). The buncher modulates the energy of the particles as shown in Fig. 8(b). The particle distribution changes into that of Fig. 8(c) in front of the linear accelerator at z_3 where a large part of the particles is bunched in a phase focus. Thus, a larger fraction of the protons is redistributed around the zero phase $\varphi = 0°$. That part is well accepted by the linac when the phase of the buncher is well adjusted to the phase of the linac. The energy modulation by the buncher leads to an increased energy spread of the beam of $\Delta E/E_0 = \pm 0.125\%$ (still accepted by the linac) while the fraction of particles fitting the phase accepted by the linac is increased. In total, the modulated beam fits better to the longitudinal acceptance of the linac as represented by the particle distribution from the acceptance study [gray dots in Fig. 8(c)].

The longitudinal phase space distribution of the 70 MeV protons after the linac at z_4 is depicted in Fig. 9(a) together with its transverse *X-Y* projection in Fig. 9(b) and the transverse *X–X′/Y–Y′* projections in Figs. 9(c)/9(d). The relative energy spread is enlarged to $\Delta E/E_0 = \pm 0.13\%$ (FWHM). A total fraction of 52% of the protons from the tandem is

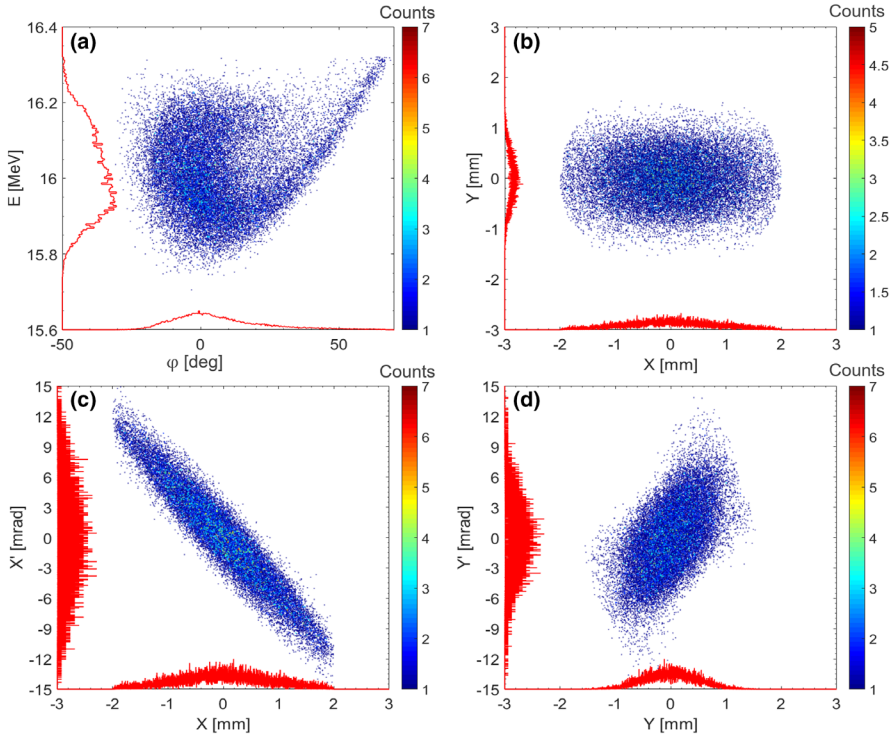

FIG. 5. Two-dimensional projections of the six-dimensional accepted phase space of the linear accelerator at position z_3. (a) φ-E, (b) *X-Y*, (c) *X–X′*, (d) *Y–Y′*. [Color figure can be viewed at wileyonlinelibrary.com]

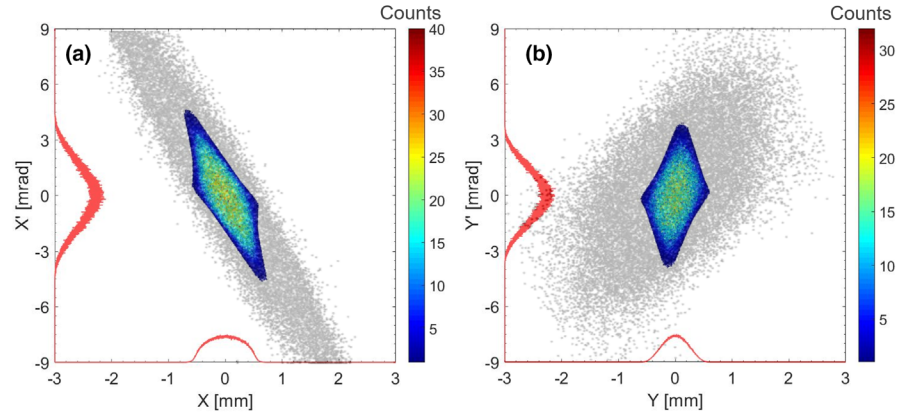

FIG. 6. Two-dimensional projections of the transverse phase space of the protons from the tandem accelerator as transferred to the entrance of the linear accelerator (z_3) using the setting of the quadrupole quadruplet at z_2 as shown in Fig. 7. (a): X–X' projection, (b): Y–Y' projection (colored). In gray, the transverse phase space accepted by the linac is represented by the distribution of protons transmitted through the linac, taken from Fig. 5(a,b).

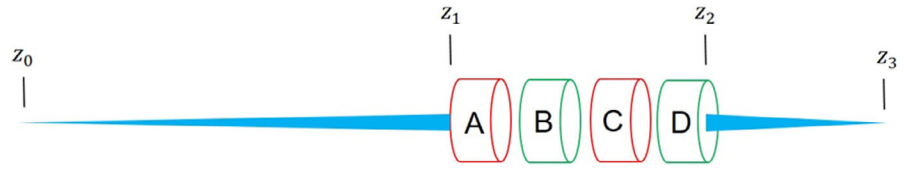

FIG. 7. Sketch of the focusing structure between buncher and linac. [Color figure can be viewed at wileyonlinelibrary.com]

transmitted through the linac and a beam size of about 0.44 mm (mean value of X- and Y-projection of the 6D particle distribution) is achieved. The divergences X' and Y' for 50% and 90% of all particles at position z_4 are $X'_{50\%}$ = 1.1 mrad, $X'_{90\%}$ = 1.9 mrad, $Y'_{50\%}$ = 1.1 mrad, and $Y'_{90\%}$ = 2.0 mrad.

The beam is focused by means of the quadrupole triplet after the linac situated at z_5 to the focal plane at z_7. The resulting particle distribution in the transverse phase space is plotted in Fig. 10. The parameters of the optimized lens settings corresponding to this particle distribution are shown in Fig. 11 and Table III. The total percentage of particles transported from the tandem through the linac into an area of 0.1 × 0.1 mm^2 in the focus z_7 is 39% with a transmission from the end of the linac (z_4) to the focal plane (z_7) of 75%. Simulation with a reduced energy distribution at z_4 considering only protons with (70.25 ± 0.005) MeV shows that 20% out of the total 25% loss is due to the chosen dimension of the drift length z_{67} and the thereby limited demagnification. The halo around the focus point, representing 5% of the particles results from chromatic aberration of the quadrupole triplet (see Fig. 11) due to the energy spread $\Delta E/E_0$ of ±0.13 % FWHM.

TABLE II. Parameters of the focusing structure between buncher and linac for the buncher configuration U_b = 35 kV that produces a longitudinal focus at the linac entrance z_3. A negative gradient corresponds to a vertically focusing quadrupole, a positive gradient to a horizontally focusing quadrupole.

Element name	Element type	Length [m]	Gradient [T/m]
Z_{01}	Drift space	1.52	
Quad A	Quadrupole	0.15	−22.00
Z_{AB}	Drift space	0.2	
Quad B	Quadrupole	0.15	19.52
Z_{BC}	Drift space	0.2	
Quad C	Quadrupole	0.15	−19.95
Z_{CD}	Drift space	0.2	
Quad D	Quadrupole	0.15	24.09
Z_{23}	Drift space	0.55	

The influence on the beam dimensions caused by the space charge effect can be described by the perveance K.[34] The maximum, $K = \frac{I_B}{U^{\frac{3}{2}}} \approx 6.2 \cdot 10^{-19} \frac{A}{V^{\frac{3}{2}}}$ is reached between z_0 and z_3 where the relation of beam radius r to distance z reads as:

$$r(z) = \sqrt{\frac{K}{4\pi\varepsilon_0\sqrt{\frac{2q}{m}}}} \cdot z = 6.4 \cdot 10^{-7} \cdot z \qquad (5)$$

Taking into account the length z_{07} = 17 m, r is increased by 10 µm. Space charge effects can thus be neglected.

3.B. Buncher optimization

To obtain the best focusing options and to reduce the beam halo as much as possible, the buncher parameters were optimized utilizing the particle tracking code TRAVEL. The buncher is used to maximize the number of particles fitting the longitudinal acceptance of the linear accelerator. Without the buncher, the simulation shows that only 14.5% of all protons delivered by the DC beam of the tandem are transported through the linac. This value corresponds to about $\Delta\varphi$ =

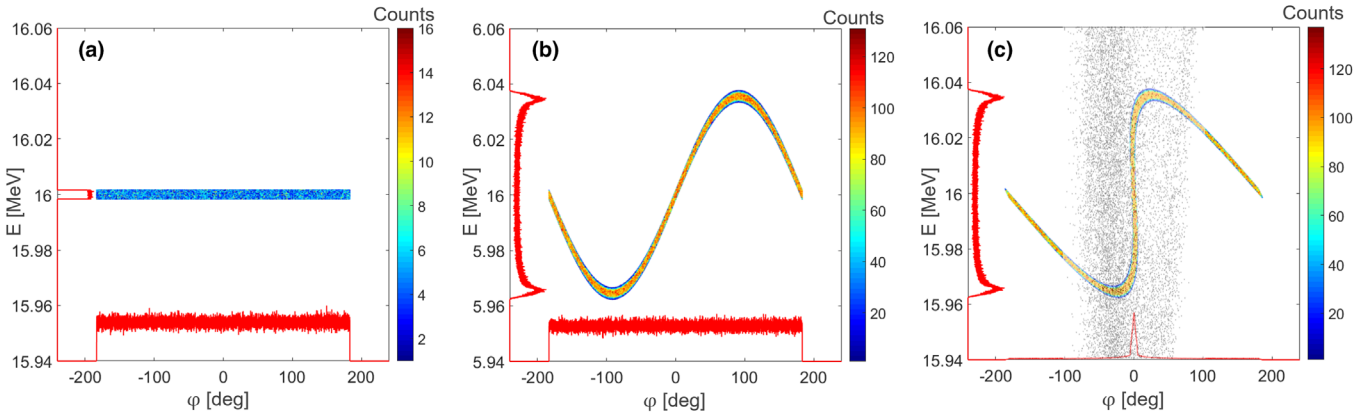

FIG. 8. (a) Longitudinal phase space of the continuous wave tandem particle beam (E_{kin} = 16 MeV, $\Delta E/E_0 = \pm 0.01\%$, $\Delta\varphi = \pm 180°$) in front of and (b) after the buncher (buncher amplitude U_B = 35 kV). (c) Longitudinal phase space at the entrance of the linear accelerator at z_3 (where there is a focus in phase). The red curves represent the projections showing the widened energy spread ($\Delta E/E_0 = \pm 0.125\%$) after the buncher (b and c). Close to 50% of the particles from the tandem forming the phase and thus time focus at z_3 (c). Besides, the longitudinal phase space accepted by the linac is plotted (in gray), representing the proton distribution as shown in Fig. 5.

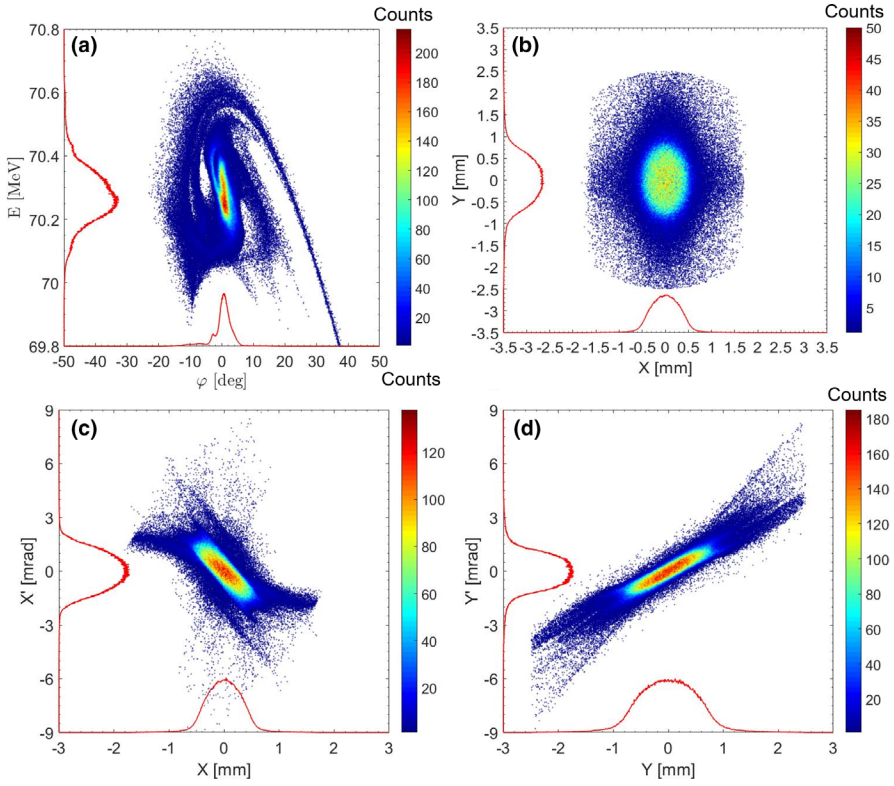

FIG. 9. Two-dimensional projections of the six-dimensional accepted phase space of the linear accelerator at position z_4. (a) φ - E shows an energy spread $\Delta E/E_0$ of approx. ± 0.13% FWHM, (b) *X-Y* shows a beam size of about 0.44 mm (mean value of X- and Y-projection of the six-dimensional particle distribution), (c) *X–X′* shows $X'_{50\%}$ = 1.1 mrad and $X'_{90\%}$ = 1.9 mrad divergences for 50% and 90% of all particles at position z_4, and (d) *Y–Y′* shows $Y'_{50\%}$ = 1.1 mrad and $Y'_{90\%}$ = 2.0 mrad divergences for 50% and 90% of all particles at position z_4. Buncher configuration: U_b = 35 kV, and time focus at the entrance of the linac structure (z_3). [Color figure can be viewed at wileyonlinelibrary.com]

±27° phase acceptance of the post-accelerator (close to the value as simulated by Picardi et al. for the TOP-IMPLART accelerator[22]). The rest of the protons would be lost in the linac. By including the buncher, nearly half the beam current from the tandem can be compressed into the longitudinal acceptance of the post-accelerator (see Fig. 8). Here, however, the transmission into the 0.1 × 0.1 mm^2 was the criterion to optimize the buncher amplitude U_b, the distance between buncher (z_0) and the entrance of the linac (z_3), and the relative phase of the buncher and linac. For this purpose, the amplitude U_b was varied from 10 to 100 kV [Fig. 12(a)]. For every variation of the buncher amplitude U_b, the drift

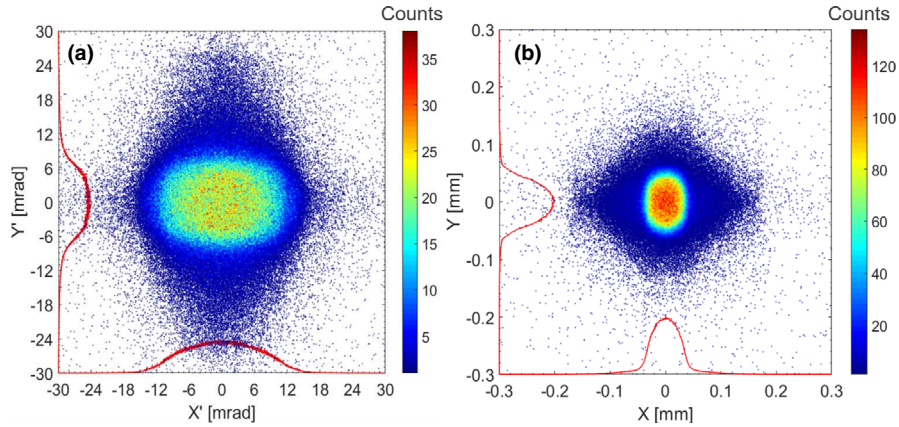

FIG. 10. Two-dimensional projections of the transverse phase space at focus z_7 with 40% of all protons from the tandem in an area of 100 × 100 μm. Buncher configuration: U_b = 35 kV and longitudinal focus at z_3. Focused by the imaging system described in Fig. 11. (a) X'–Y' (b) X–Y. [Color figure can be viewed at wileyonlinelibrary.com]

FIG. 11. Sketch of the focusing system consisting of a quadrupole triplet and two drift lengths after the linear accelerator for the buncher configuration U_b = 35 kV and longitudinal focus at the input to linac structure. At the maximum beam size within the lenses, 90% of the particles fit into a circular aperture with a diameter of 44 mm. [Color figure can be viewed at wileyonlinelibrary.com]

distances between buncher and linac (z_{03}), quadrupole quadruplet and linac (z_{23}) as well as the magnetic field strengths of the quadrupole quadruplet (z_{12}) and the quadrupole triplet at z_{56} were optimized with TRACE-3D.

In general, below U_b ~ 20 kV, the transmission through the linear accelerator decreases rapidly [Fig. 12(a)]. This is due to poor focusing in the longitudinal plane. An extreme case is shown for a buncher amplitude of 10 kV [Fig. 12(b)]. For a buncher amplitude higher than U_b ~ 40 kV, the number of protons transmitted into an area of 0.1 × 0.1 mm^2 also decreases mainly due to increased chromatic aberration of the quadrupole triplet (at z_5), caused by the energy spread $\Delta E/E$, which is ±0.6% for U_b = 100 kV [Fig. 12(c)]. In conclusion, a buncher amplitude in the range between U_b ~ 20 kV and U_b ~ 40 kV results in almost constant proton transmission into an area of 0.1 × 0.1 mm^2 at the focus z_7 with an overall transmission of about 35%. Therefore, the 3.27 m (z_{03}) long focusing structure between buncher and linac as shown in Fig. 7 and described in Table II meets the requirements for an efficient beam transmission through the linac. The final study optimizes the buncher amplitude U_b and the phase shift $\Delta\varphi_s$ between buncher and linac and thus the tilt of the proton distribution in the longitudinal E-φ phase space distribution at the entrance to the linac (z_3). The buncher to linac distance of z_{03} = 3.27 m is taken constant. Optimization is done with respect to the smallest full width half maximum and smallest beam halo at the focus point z_7. A series of simulations were performed for phase shifts between $\Delta\varphi_s$ = −3° and $\Delta\varphi_s$ = 8° and buncher amplitudes from U_b = 35 kV to U_b = 47 kV. The zero phase in the longitudinal phase space is in the centroid of the proton distribution. The phase $\Delta\varphi_s$ shift between the particle bunch (z_1) and the center of the accepted phase space by the linac (z_3) is achieved by offsetting each proton in the longitudinal phase by the desired phase shift of the buncher at z_0. Figure 13 shows the proton transmission at E = 70 MeV into an area of (0.1 × 0.1) mm^2 at z_7 with a maximum total transmission of 47% of all protons injected from the tandem when using $\Delta\varphi_s$ = +4° or $\Delta\varphi_s$ = +6° and U_b = 42 kV or U_b = 43 kV. Thus, a transmitted average beam current of about 19 nA is expected in the final spot with beam divergences of $X'_{50\%}$ = 5.1 mrad, $X'_{90\%}$ = 12.2 mrad, $Y'_{50\%}$ = 5.2 mrad,

TABLE III. Parameters of the focusing system after the linear accelerator for the buncher configuration U_b = 35 kV and longitudinal focus at the input to linac structure. A negative gradient corresponds to a vertically focusing quadrupole, a positive gradient to a horizontally focusing quadrupole.

Element name	Element type	Length [m]	Gradient [T/m]
Z_{4E}	Drift space	6	
Quad E	Quadrupole	0.1	−18.52
Z_{EF}	Drift space	0.2	
Quad F	Quadrupole	0.2	18.52
Z_{FG}	Drift space	0.2	
Quad G	Quadrupole	0.1	−28.58
Z_{G7}	Drift space	0.6	

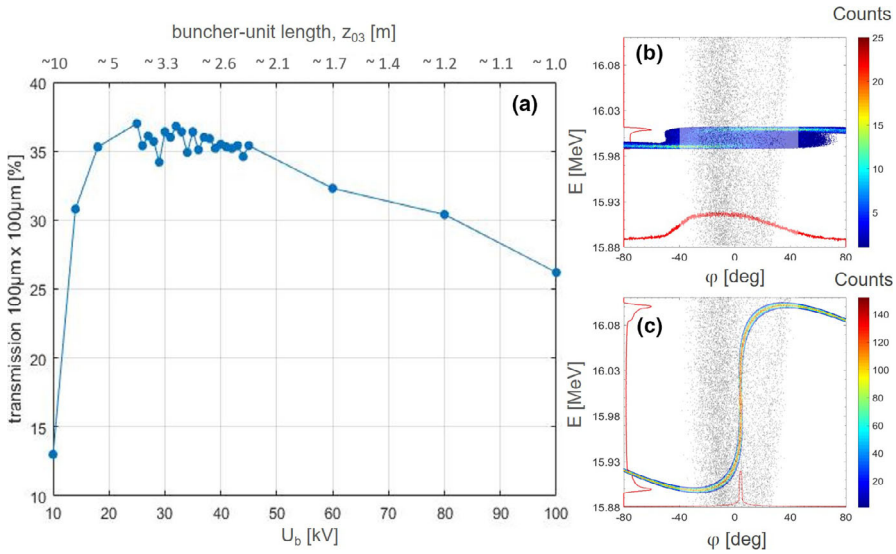

FIG. 12. a) Transmission from the tandem into the 0.1 × 0.1 mm^2 field at z_7 for different buncher amplitudes U_b and the corresponding drift distances between buncher and linac (z_{03}). Drift distances between quadrupole quadruplet and linac (z_{23}), magnetic field strengths of the quadrupole quadruplet at z_{12}, and quadrupole triplet (z_{56}) were adapted for each U_b to optimize the transmission in 0.1 × 0.1 mm^2. (b) Particle distribution of the longitudinal phase space at z_3 for a buncher-unit length of z_{03} = 9.8 m and U_b = 10 kV. (c) Same as (b) for z_{03} = 0.82 m and U_b = 100 kV. The total longitudinal phase space accepted by the linac is given by the gray dots representing all particles accepted by the linac from Fig. 5.

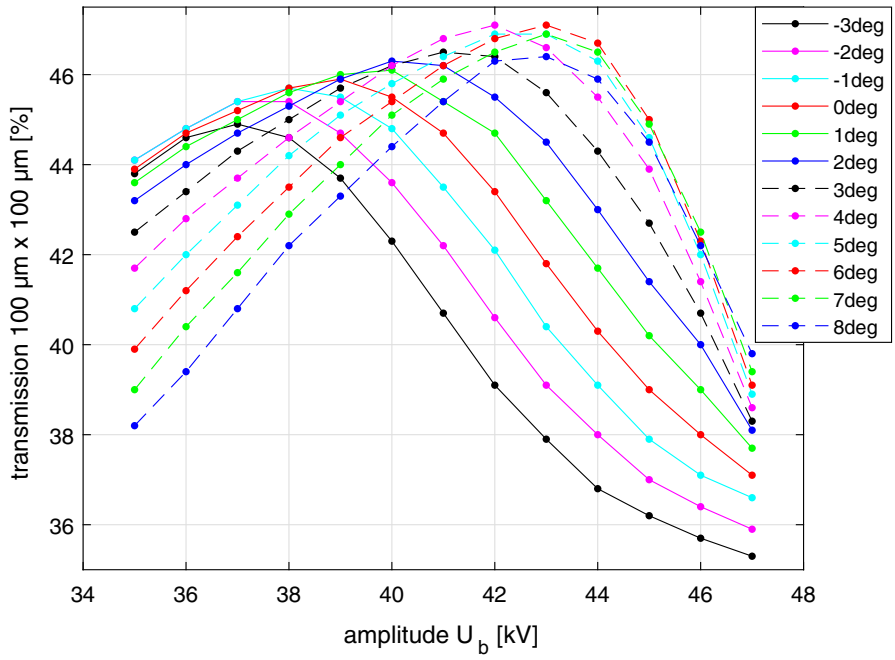

FIG. 13. Overall proton transmission into an area of (100 × 100) µm at z_7 in dependence of buncher amplitude U_b calculated for various phase shifts $\Delta\varphi_s$ for a buncher–linac distance z_{13} = 3.27 m.

$Y'_{90\%}$ = 10.1 mrad (respectively, for the envelopes including 50% and 90% of all particles at position z_7).

The maximum was confirmed by the smallest full width half maximum of the particle distribution as well as in the smallest halo. In order to show the sensitivity in the two parameters, examples of the particle distributions are shown for three settings in Fig. 14(a) for the divergence X' and Fig. 14(b) for the X-dimension (1: $\Delta\varphi_s = 8°$, U_b = 35 kV; 2: $\Delta\varphi_s = 4°$, U_b = 42 kV; 3: $\Delta\varphi_s = -3°$, U_b = 47 kV).

After optimizing the beam transport system, the influence of dispersion, caused by the 90° magnet in front of position z_0, on the beam spot size and transmission into an area of (0.1 × 0.1) mm^2 at z_7 was evaluated. Therefore, the 90° magnet, as it is located in the accelerator laboratory in Garching, was integrated into the travel particle tracking simulations. The magnet is double focusing (edge angles: 26.5°), has a deflection radius of 1.65 m and a (full) pole gap of 60 mm. The distance between the focus points and the 90° magnet is

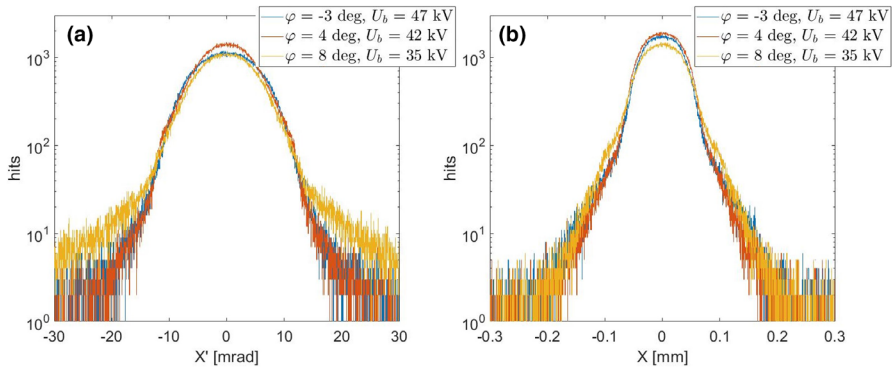

FIG. 14. Distribution of particles at point z_7 as a histogram for different buncher configurations. Blue: $\Delta\varphi_s = 8°$, $U_b = 35$ kV, orange: $\Delta\varphi_s = 4°$, $U_b = 42$ kV, and yellow: $\Delta\varphi_s = -3°$, $U_b = 47$ kV. (a) *X*'-projection of the transverse phase space, (b) X-projection of the transverse phase space.

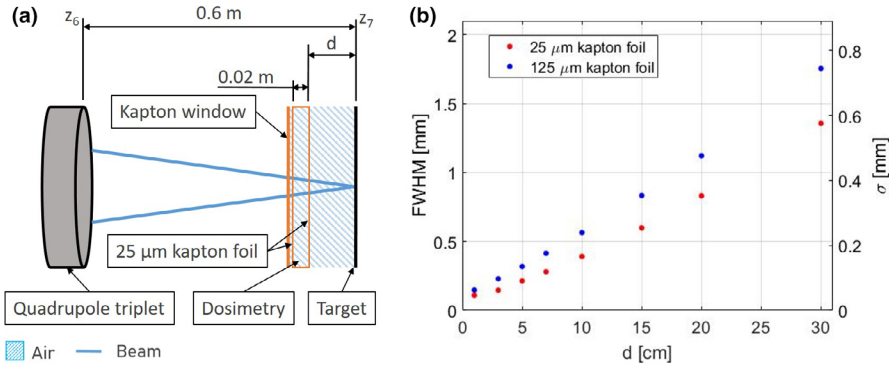

FIG. 15. (a) Sketch of the beam line elements after the last focusing lens. (b) TOPAS simulation of the 70 MeV minibeam sizes at the focus (z_7) in dependence of the gap thickness d caused by the elements depicted in (a). σ and FWHM values at the beam focus (z_7) are shown for a 25 and 125 µm kapton extraction foil. [Color figure can be viewed at wileyonlinelibrary.com]

3.3 m. The initial phase space (equal to the one shown in Fig. 4) is now located at the focus point upstream of the 90° magnet. The focus point downstream of the 90° magnet is at position z_0. Three buncher configurations were considered (1: $\Delta\varphi_s = 8°$, $U_b = 35$ kV; 2: $\Delta\varphi_s = 4°$, $U_b = 42$ kV; 3: $\Delta\varphi_s = -3°$, $U_b = 47$ kV).

No significant changes were found in either transmission [into an area of (0.1×0.1) mm^2] or in the beam size at the focus plane z_7 compared to the simulations without the 90° magnet (see Figs. 13 and 14).

3.C. Beam extraction and scanning

To complete the conceptual study, in this section, considerations about the beam extraction and beam scanning are presented. In order to apply the minibeams in preclinical experiments, the beam has to be extracted to air before hitting the target (e.g., small animal) situated at the focus plane z_7 [see Fig. 15(a)]. A vacuum window and a small dosimetry unit are considered. Furthermore, a scanning system is studied to distribute the dose over the target. The planned field size of 30 mm × 30 mm, sufficient for preclinical minibeam studies, defines the requirements for the scanning system and the vacuum window.

3.C.1. Beam extraction

25 µm thick kapton foils have already been used in radiobiological studies for beam exit windows of up to 60 mm in diameter which is easily sufficient to cover the planned field size of 30 mm × 30 mm.[35] Nevertheless, both a 25 and a 125 µm thick kapton window are investigated as extraction windows with respect to the lateral propagation of the proton minibeam at the focal point. In addition, the lateral spread from a dosimetry unit and from the protons traversing through air is considered. The dosimetry unit consists of two 25 µm kapton foils with a gap of 2 cm filled with air situated directly behind the extraction window. The air could be replaced by a gas of light atoms or molecules (e.g., helium or methane gas) to reduce lateral spread. A comparable dosimetry unit similar to the ionization chamber-based energy detector as published by Eschbaumer et al.[36] has already been used in preclinical experiments.

A series of simulations was elaborated with TOPAS to determine the overall lateral proton distribution of a 70 MeV beam at the beam focus (z_7) in dependence of the distance *d* between dosimetry unit and focus. The initial 6D phase space of these simulations corresponds to the 6D phase space at point z_6 of the TRAVEL simulations. Beam sizes in the *X-Y*

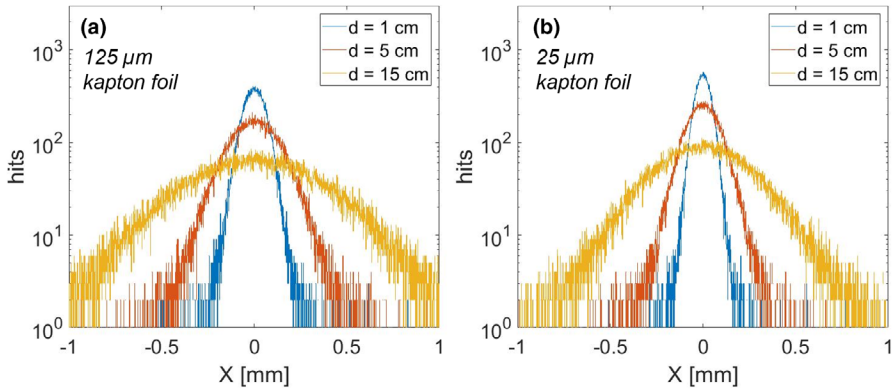

FIG. 16. Spatial particle distributions for different distances d between dosimetry unit and focus point (z_7) at point z_7. (a) shows the particle distributions for the 125 µm (b) for the 25 µm kapton extraction foil.

plane are presented as full width half maximum (*FWHM*) and σ values in Fig. 15(b). The resulting particle distributions at the focus (z_7) for $d = 1$ cm, $d = 5$ cm, and $d = 15$ cm are shown in Fig. 16(a) in case of the 125 µm kapton foil and in Fig. 16(b) for the 25 µm kapton foil. Beam sizes < 90 µm are obtained for distances d smaller than 3 and 5 cm for extraction foil thicknesses of 125 and 25 µm, respectively. These small beam sizes caused negligible side effects when applied in a grid with center to center distances of 1.8 mm in a mouse ear model but side effects increased when using larger beam sizes. Thus, the proposed accelerator and beam focusing system including the extraction unit is a suitable setup to perform preclinical proton minibeam irradiation experiments.

The spread of a 70 MeV proton beam resulting from multiple small-angle scattering within tissues was simulated with TOPAS in a water phantom. After a distance of 4 cm in water, that is nearly the range of the 70 MeV protons, a width of $\sigma = 0.61$ mm was determined for a point-like parallel beam, that is, of infinitely small size and zero divergence at the surface of the water surface. The beam as simulated for the preclinical radiation facility (extraction foil thickness of 25 µm and a distance $d = 1$ cm) (see Fig. 15) spreads to $\sigma = 0.65$ mm after a distance of 4 cm in water. The beam size of 44 µm (25 µm Kapton, d = 1 cm) as provided by the preclinical irradiation facility at the entrance to the phantom is negligible compared to the beam propagation when superimposed added in quadrature. The comparison with the point-like parallel beam shows that the contribution of the initial divergence of the beam (at z_7) as simulated for the preclinical irradiation facility to the spread is small. The beam divergence at z_7 can be further reduced by apertures between z_4 and z_5 at the cost of reduced beam current.

To estimate the change of the peak-to-valley dose ratio (PVDR) caused by secondary radiation (resulting from the exit window and dosimetry unit), a basic minibeam application using 170 minibeams (similar to the one shown in Fig. 1) is simulated with TOPAS. The geometry of the minibeam array and the water phantom corresponds to the arrangement shown in Fig. 1, but the phantom ($z = 0$ mm) is now situated at point z_7. Therefore, instead of using Gaussian beams without initial divergence (like in Fig. 1), the phantom is irradiated with an array of $\sigma = 85$ µm minibeams as simulated for the preclinical irradiation facility ($d = 5$ cm, 25 µm thick kapton window). Dose uniformity ($0.95 \cdot D < D < 1.07 \cdot D$) is again obtained in the target area at $Z = 34$ mm (white dashed line) like for the Gaussian beams without initial divergence (see Fig. 1).

Figure 17 show the lateral dose distributions from projections at z = 0 for Gaussian minibeams without initial divergence as calculated for Fig. 1 (orange line) and, respectively, the beams simulated for the preclinical irradiation facility (blue line). The projections are plotted for the dose distributions between the two dashed green lines in Fig. 1(b). A PVDR of 780 results at the entrance of the phantom in case of the 70 MeV proton beam from the preclinical irradiation facility. Compared to the Gaussian minibeams without initial divergence, the PVDR is reduced by a factor approx. 13. The calculated PVDR is more than an order of magnitude larger than those obtained from proton minibeam formed by collimators.[37,38]

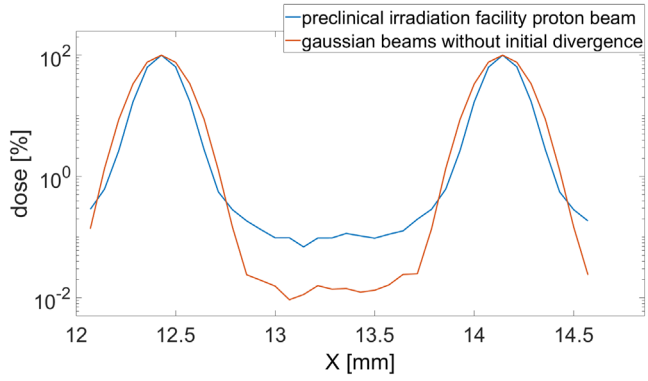

FIG. 17. Dose distribution in X direction at Z = 0 between the two green lines marked in Fig. 1(b). Orange: Gaussian beams without initial divergence (see Fig. 1). Blue: dose distribution in X direction at Z = 0 as simulated with TOPAS for a minibeam application with a quadratic grid array of 170 minibeams (ctc 1.2 mm) of 70 MeV protons as simulated for the preclinical irradiation facility. Using a target to dosimetry unit distance d = 5 cm and a 25 µm thick kapton extraction window, a beam size of 85 µm is obtained. Geometry of the water phantom and minibeam array corresponds to Fig. 1.

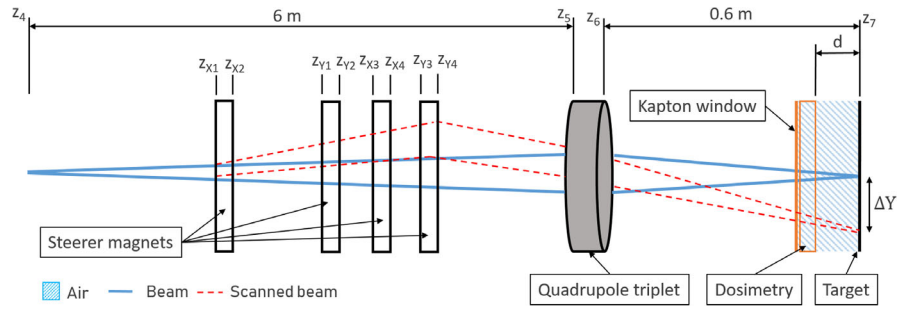

FIG. 18. Sketch of the beam extraction and the scanning unit. A kapton extraction window provides the vacuum barrier. An arrangement of two 25 μm kapton foils, separated by 2 cm air, serves as a dosimetry unit. Four scanning magnets are placed between linac and quadrupole triplet allowing to scan the proton beam over the target. The blue lines represent the proton beam without deflection by the scanning magnets. The red dotted lines illustrate the deflection by the scanning magnets during the scanning process. [Color figure can be viewed at wileyonlinelibrary.com]

3.C.2. Beam scanning

For beam scanning, a scanning unit consisting of four scanning magnets is placed between the linac and the quadrupole triplet along the line segment z_{45} (see Fig. 18). Dimensions and positions of the magnets are summarized in Table IV together with the field strengths of the magnets as required to cover a field size of 30 mm × 30 mm. Scanning magnets with higher field strengths and comparable dimensions have already been used in proton therapy systems, making the assumed values (Table IV) feasible.[39] The pairwise arrangement of the magnets for scanning in X and Y allows the proton beam to pass the quadrupole triplet as close as possible to the optical axis. Such an arrangement of the scanning magnets has already been proposed by Pavlovic et al.[40] Figure 19 shows the particle distributions in X and Y at z_7 for a deflection of $\Delta X = 15$ mm and $\Delta Y = -15$ mm in (a) and $\Delta X = -15$ mm and $\Delta Y = 0$ mm in (b). The resulting sigma of the minibeam is 87 μm in (a) and 87 μm in (b). Thus, beam sizes < 90 μm are also obtained for the spot scanning process at a distance of $d = 5$ cm and 25 μm kapton extraction foil.

3.D. RFQ–linac arrangement

For comparison with the tandem–linac combination, the beam parameters are also calculated for the commercially available RFQ–linac combination[20,27] limited at 70 MeV. The 6D phase space of the proton beam at the end of the fourth CCL structure of the LIGHT prototype as provided by AVO-ADAM S.A is used at z_4.

TABLE IV. Parameters of the scanning unit consisting of four scanning magnets placed between the linac and the quadrupole triplet.

Element name	Element type	Length [m]	Magnetic field [mT]
Z_{4X1}	Drift space	3.95	
Z_{X1X2}	Scanning magnet	0.1	150
Z_{X2Y1}	Drift space	0.6	
Z_{Y1Y2}	Scanning magnet	0.1	160
Z_{Y2X3}	Drift space	0.2	
Z_{X3X4}	Scanning magnet	0.1	300
Z_{X4Y3}	Drift space	0.2	
Z_{X3Y4}	Scanning magnet	0.1	310
Z_{Y45}	Drift space	0.65	

An average beam current of 39 nA can be expected for 5 μs long pulses at 200 Hz repetition rate after the SCDTL Module 2.[21] The same 39 nA beam current is assumed at point z_4 since no particle losses are expected for the further beam transport. The proton beam as propagated from z_4 is focused by the quadrupole triplet at point z_5 to the focal plane at z_7 where the geometrical parameters of the arrangement between z_4 and z_7 (Fig. 3) correspond to those presented in Table III. To maximize the percentage of focused protons in a square of 0.1 × 0.1 mm^2, the field strengths of the three quadrupole magnets were modified (Table V). At the maximum beam size within the lenses, 90% of the particles fit into a circular aperture with a diameter of 40 mm.

The resulting particle distribution in the focal plane at z_7 is plotted in Fig. 20. The percentage of particles focused on an area of 0.1 × 0.1 mm^2 is 96%. Thus, an average beam current of 37 nA is expected in the final spot with beam divergences of $X'_{50\%} = 4.9$ mrad, $X'_{90\%} = 8.5$ mrad, $Y'_{50\%} = 5.4$ mrad, $Y'_{90\%} = 10.2$ mrad, respectively (including 50% and 90% of all particles at position z_7). Figure 21 shows the histograms of the X' and X particle distributions at the beam focus (z_7) without considering the extraction unit. The beam divergence is comparable to that of the tandem linac approach, while the halo is reduced. It can be assumed that the beam characteristics after extraction as described in chapter 3.3 will be sufficient for preclinical proton minibeam irradiation.

4. CONCLUSION

The beam transport simulations demonstrate that a 16 MeV proton beam from a tandem accelerator can be well fitted into a linac structure consisting of 3 GHz SCDTL and CCL cavities to obtain 70 MeV proton energy. By utilizing a buncher and a quadrupole quadruplet in front of the linac, it is possible to transport nearly 50% of the DC tandem beam through the linac and into a

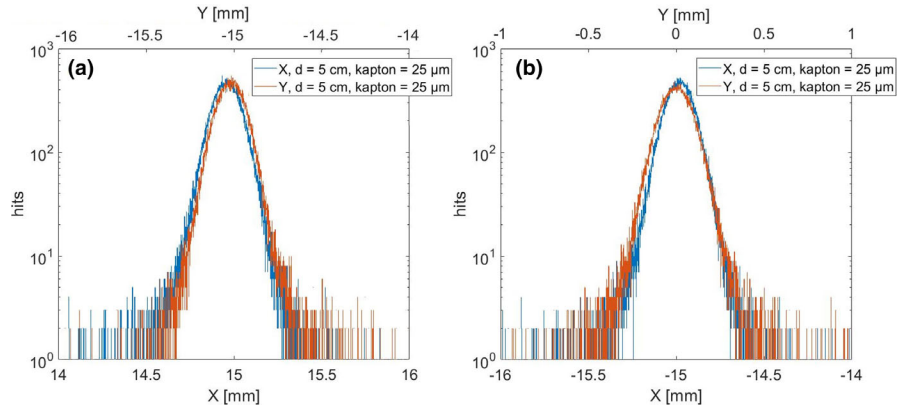

FIG. 19. Particle distributions in X and Y at z_7 for a deflection of (a) $\Delta X = 15$ mm and $\Delta Y = -15$ mm and (b) $\Delta X = -15$ mm and $\Delta Y = 0$ mm for a distance of d = 3 cm and 25 µm kapton extraction foil. [Color figure can be viewed at wileyonlinelibrary.com]

TABLE V. Modified magnetic field strengths of the quadrupole triplet located at point z_5 to be used for the RFQ–linac combination for an optimized beam focus at z_7. A negative gradient corresponds to a vertically focusing quadrupole, a positive gradient to a horizontally focusing quadrupole.

Element name	Gradient [T/m]
Quad E	18.76
Quad F	−18.76
Quad G	30.03

0.1×0.1 mm^2 area with small halo using an additional quadrupole triplet after the linac. The magnetic focusing makes possible to perform minibeam irradiation with high peak-to-valley dose ratio at proton currents up to 19 nA (5 µs at 200 Hz). Considering the reduction of the effective pulse length to 3 µs due to the filling time and the currently used RF source, a beam current of 11 nA would result. Nevertheless, the requirements for proton beam current at the target can be met.

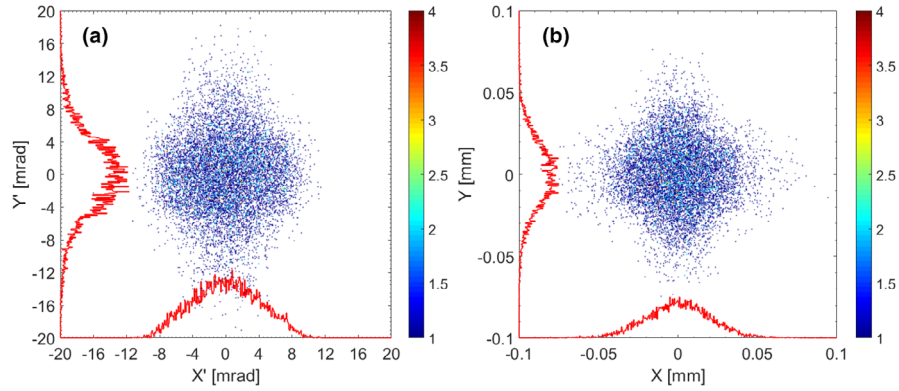

FIG. 20. Two-dimensional projections of the transverse phase space of 70 MeV protons from an RFQ–linac accelerator at z_7. 96% of the protons (at position z_7) are found in an area of 100×100 µm. Focused by the imaging system described in Fig. 11 modified according to Table V. (a) X'–Y' (b) X–Y.

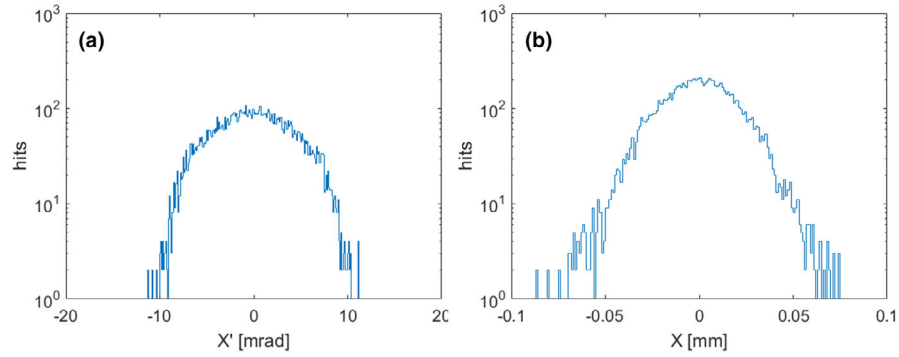

FIG. 21. Particle distributions at point z_7. (a) X'-projection of the transverse phase space, (b) X-projection of the transverse phase space. [Color figure can be viewed at wileyonlinelibrary.com]

The beam brightness from the tandem–linac combination is within a factor of 2 of that available at an RFQ–linac. Cyclotron or synchrotron-based clinical accelerators are not able to provide such a high brightness at 70 MeV. The tandem–linac combination has the additional advantage that the high beam quality of the stand-alone tandem accelerator (protons and heavy ions) can be used for other purposes, for example, for materials sciences or other radiobiological experiments such as serving an ion microbeam.[41–43]

The tandem–linac combination is a cost-effective option to obtain a preclinical proton minibeam facility when utilizing an existing tandem accelerator delivering 16 MeV protons as an injector. Thus, the source and RFQ devices as required for an all-linac system can be spared. Similarly, even smaller tandem accelerators delivering proton beams above 5 MeV can be utilized as injectors when setting additional SCDTL-structures at the low energy side of the linac.

In total, a linac structure (like the one of the TOP-IMPLART or the LIGHT project) served by a tandem accelerator or an RFQ offers high beam brightness and thus is well suited to evaluate the potential of tumor irradiation utilizing spatial fractionation through proton minibeams. The introduction of beam scanning, beam extraction to air, and beam diagnostics has been studied. The distance between exit nozzle and beam applications must be kept in the order of 5 cm to achieve beam sizes as small as 0.09 mm (25 μm kapton foil) at the focus. Although, such an air gap is much lower than it is used in conventional proton or heavy ion irradiation facilities, for a dedicated preclinical proton minibeam irradiation stage, the small nozzle–target distance can be taken into account.

The tandem–linac combination as described here can be extended by further 3 GHz CCL structures as suggested in the TOP-IMPLART or in the LIGHT project in order to reach even higher proton energies (e.g., 150 MeV or even 230 MeV). We expect the tandem–linac combination to result in similar beam brightness as from the original LIGHT project.[21]

CONFLICT OF INTEREST

The authors have no relevant conflict of interest to disclose.

DATA AVAILABILITY STATEMENT

The data that support the findings of this study are available from the corresponding author upon reasonable request.

[a]Author to whom correspondence should be addressed. Electronic mail: michael.mayerhofer@unibw.de; Telephone: +49 (0) 89 6004 3515; Fax: +49 (0) 89 6004 3295.

REFERENCES

1. Jemal A, Siegel R, Ward E, et al. Cancer statistics, 2006. *CA: A Cancer Journal for Clinicians*. 2006;56:106–130.
2. Kauffmann G, Sauer R, Weber W, Dangl S. *Radiologie: Bildgebende Verfahren, Strahlentherapie, Nuklearmedizin und Strahlenschutz*. Elsevier Health Sciences; 2013.
3. Bragg WH, Kleeman R. XXXIX. On the α particles of radium, and their loss of range in passing through various atoms and molecules. *London, Edinburgh, and Dublin Phil Magaz J Sci*. 1905;10:318–340.
4. Paganetti H, Bortfeld T, Kooy H. Proton beam radiotherapy: the state of the art. *Med Phys*. 2005;32:2048–2049.
5. Zlobinskaya O, Girst S, Greubel C, et al. Reduced side effects by proton microchannel radiotherapy: study in a human skin model. *Radiat Environ Biophys*. 2013;52:123–133.
6. Prezado Y, Fois GR. Proton-minibeam radiation therapy: a proof of concept. *Med Phys*. 2013;40:31712.
7. Sammer et al. Submitted. Scientific reports. 2020.
8. Sammer M, Greubel C, Girst S, Dollinger G. Optimization of beam arrangements in proton minibeam radiotherapy by cell survival simulations. *Med Phys*. 2017;44:6096–6104.
9. Girst S, Greubel C, Reindl J, et al. Proton minibeam radiation therapy reduces side effects in an in vivo mouse ear model. *Int J Radiat Oncol Biol Phys*. 2016;95:234–241.
10. Prezado Y, Jouvion G, Hardy D, et al. Proton minibeam radiation therapy spares normal rat brain: long-term clinical, radiological and histopathological analysis. *Sci Rep*. 2017;7:14403.
11. Sammer M, Zahnbrecher E, Dobiasch S, et al. Proton pencil minibeam irradiation of an in-vivo mouse ear model spares healthy tissue dependent on beam size. *PLoS One*. 2019;14:e0224873.
12. Sammer M, Teiluf K, Girst S, et al. Beam size limit for pencil minibeam radiotherapy determined from side effects in an in-vivo mouse ear model. *PLoS One*. 2019;14:e0221454.
13. Datzmann G, Sammer M, Girst S, Mayerhofer M, Dollinger G, Reindl J. Preclinical challenges in proton minibeam radiotherapy: physics and biomedical aspects. *Front Phys*. 2020;8:4–6.
14. Schneider T, de Marzi L, Patriarca A, Prezado Y. Advancing proton minibeam radiation therapy: magnetically focussed proton minibeams at a clinical centre. *Sci Rep*. 2020;10:1–10.
15. Perl J, Shin J, Schümann J, Faddegon B, Paganetti H. TOPAS: an innovative proton Monte Carlo platform for research and clinical applications. *Med Phys*. 2012;39:6818–6837.
16. ICRU. Prescribing, recording and reporting photon beam therapy. *ICRU report 50*. 1993;50:5–7.
17. ICRU. Prescribing, recording and reporting photon beam therapy (supplement to ICRU Report 50). *ICRU report*. 1999;62:60–62.
18. Prezado Y, Deman P, Varlet P, et al. Tolerance to dose escalation in minibeam radiation therapy applied to normal rat brain: long-term clinical, radiological and histopathological analysis. *Radiat Res*. 2015;184:314–321.
19. Prezado Y, Sarun S, Gil S, Deman P, Bouchet A, Le Duc G. Increase of lifespan for glioma-bearing rats by using minibeam radiation therapy. *J Synchrotron Radiat*. 2012;19:60–65.
20. Degiovanni A, Stabile P, Ungaro D. LIGHT: a linear accelerator for proton therapy. *Proceedings of NAPAC2016, Chicago, USA*. 2016.
21. Degiovanni A, Adam J, Aguilera Murciano D, et al. Status of the Commissioning of the LIGHT Prototype. In: 9th Int. Particle Accelerator Conf.(IPAC'18), Vancouver, BC, Canada, April 29-May 4, 2018; 2018:425–428.
22. Picardi L, Ronsivalle C, Vignati A. PROGETTO DI Acceleratore COMPATTO PER TERAPIA ONCOLOGICA CON PROTONI (TOP).
23. Ronsivalle C, Picardi L, Ampollini A, et al. First acceleration of a proton beam in a side coupled drift tube linac. *EPL (Europhysics Letters)*. 2015;111:14002.
24. Ziegler JF, Ziegler MD, Biersack JP. SRIM–The stopping and range of ions in matter (2010). *Nucl Instrum Methods Phys Res B*. 2010;268:1818–1823.
25. Assmann W, De Boer J, Meyer-Berkhout U, et al. The munich mp tandem. *Nucl Instrum Methods*. 1974;122:191–203.
26. Berti R. *Conditions for installing a RF linac as a post accelerator for preclinical studies using proton minibeams. Università di Pisa, Universität der Bundeswehr München*; 2019.
27. Ronsivalle C, Carpanese M, Marino C, et al. The top-implart project. *Eur Phys J Plus*. 2011;126:68.

28. Alvarez LW, Bradner H, Franck JV, et al. Berkeley proton linear accelerator. *Rev Sci Instrum*. 1955;26:111–133.
29. D'Auria G, Borsi P, Carniel A, et al. Installation and commissioning of the 100 MeV preinjector Linac of the New Elettra Injector. In: Proc. of this conference; 2008.
30. Picardi L, Ronsivalle C. Progress in the Development of the TOP Linac; 2004.
31. Mayerhofer M, Bergmaier A, Datzmann D, et al. Concept and performance evaluation of two 3 GHz buncherunits optimizing the dose rate of a novel preclinical protonminibeam irradiation facilitye. Currently under review at PLOSONE; 2021.
32. Crandall KR. Trace 3-D Documentation; 1987.
33. Perrin A, Amand J-F, Mütze T, Lallement J-B, Lanzone S. TRAVEL v4.07. *User Manuel*; 2007.
34. Großer J. *Einführung in die Teilchenoptik*. Berlin: Springer-Verlag; 2013.
35. Besserer J, de Boer J, Dellert M, et al. An irradiation facility with a vertical beam for radiobiological studies. *Nucl Instrum Methods Phys Res, Sect A*. 1999;430:154–160.
36. Eschbaumer S, Bergmaier A, Seiler D, Dollinger G. Time of flight assisted ΔE-E method for enhanced isotope separation capabilities in heavy ion elastic recoil detection analysis. *Nucl Instrum Methods Phys Res B*. 2017;406:10–14.
37. Peucelle C, Nauraye C, Patriarca A, et al. Proton minibeam radiation therapy: experimental dosimetry evaluation. *Med Phys*. 2015;42:7108–7113.
38. Guardiola C, Peucelle C, Prezado Y. Optimization of the mechanical collimation for minibeam generation in proton minibeam radiation therapy. *Med Phys*. 2017;44:1470–1478.
39. Wang P, Zheng J, Song Y, Zhang W. Design of the fast scanning magnets for SC200 proton therapy facility. *IEEE Trans Appl Supercond*. 2018;29:1–5.
40. Pavlovic M. Beam-optics study of the gantry beam delivery system for light-ion cancer therapy. *Nucl Instrum Methods Phys Res, Sect A*. 1997;399:439–454.
41. Dollinger G, Faestermann T. Physics at the Munich tandem accelerator laboratory. *Nucl Phys News*. 2018;28:5–12.
42. Hable V, Greubel C, Bergmaier A, et al. The live cell irradiation and observation setup at SNAKE. *Nucl Instrum Methods Phys Res B*. 2009;267:2090–2097.
43. Hauptner A, Dietzel S, Drexler GA, et al. Microirradiation of cells with energetic heavy ions. *Radiat Environ Biophys*. 2004;42:237–245.